Assessment of an Extended HERACLES-TDB against Experimental Data for Fission Product Chemistry under SIC- and B_4C-Related Conditions

Dowoong Hwang [a,b], Yoonhee Lee [a*]
[a]*Dept. of Energy Engineering, Korea Institute of Energy Technology,*
21 Kentech-gil, Naju-si, Jeonnam-Gwangju 58330, Republic of Korea
[b]*Dept. of Applied Plasma and Quantum Beam Engineering, Jeonbuk National University,*
567, Baekje-daero, Deokjin-gu, Jeonju, Jeonbuk State, Korea 54896
**Corresponding author: yooney@kentech.ac.kr*

Keywords : source term, fission product, control rod, chemical equilibrium, thermodynamic database

1. Introduction

Radioactive iodine is a major contributor to severe-accident radiological consequences because its impact depends on both the amount released and its chemical form during transport through the reactor coolant system and containment. Although CsI is a major iodine-bearing species under light-water-reactor accident conditions, interactions with accident-related materials can redistribute iodine from CsI into non-CsI species such as HI, I, and I_2. Because these species exhibit different transport and retention behaviors, factors controlling CsI stability are important for source-term assessment [1,2].

The Phébus FP tests showed absorber-dependent differences in gaseous iodine fractions between SIC-equipped FPT1/FPT2 and B_4C-equipped FPT3 [3,4]. CHIP showed that CsI remained stable under SIC-related conditions despite the presence of Mo, Ag, and Cd, whereas TeRRa-RBS and NUREG/CR-4963 Test 28 showed that Cs–B–O formation under boron-containing conditions decreased CsI stability and increased non-CsI gaseous iodine [5–8].

However, because each experiment covers specific compositions and thermal conditions, these observations alone do not provide a common basis for evaluating Cs-I phase and species distributions across SIC- and B_4C-related conditions. Thermodynamic equilibrium calculations using GEMS and HERACLES-TDB [9–11] provide a framework for evaluating experimentally identified reaction pathways across different chemical and thermal conditions. However, HERACLES-TDB lacks several control-rod-related species–phase combinations, particularly Cs–B–O phases, thereby excluding the corresponding cesium-redistribution pathways from the equilibrium calculation. This study therefore extends HERACLES-TDB with control-rod-related species and reaction-based representations of data–deficient Cs–B–O condensed phases. The extended HERACLES-TDB is evaluated against selected results from CHIP, TeRRa-RBS-1, and NUREG/CR-4963 Test 28 to examine how competition among cesium-bearing species affects CsI stability and iodine redistribution across control-rod-related conditions.

2. Thermodynamic Database Extension and Calculation Method

2.1 GEMS Equilibrium Calculation Framework and Scope

Thermodynamic equilibrium calculations are performed using GEMS with HERACLES-TDB, a thermodynamic database developed for high-temperature nuclear fuel and fission-product systems [9,10]. For a specified temperature, pressure, and bulk elemental composition, GEMS determines the stable phase assemblage and species amounts by minimizing the total Gibbs energy subject to elemental mass-balance constraints:

$$G(n) = \sum_j n_j \mu_j \rightarrow \min,\ An = b. \quad (1)$$

where n_j and μ_j denote the amount and chemical potential of species j, respectively, A is the stoichiometric matrix, and b is the bulk elemental composition. The calculated equilibrium is therefore constrained by the species and phases included in each defined chemical system.

Each evaluation condition is treated as an independent, spatially lumped equilibrium state using the temperature, pressure, and bulk elemental composition defined based on the corresponding experimental conditions and reported data. The calculations therefore describe equilibrium competition among the phases and species included in each chemical system. Reaction kinetics, spatial transport, deposition, and time-dependent revaporization are outside the present calculation scope. The case-specific input conditions and comparison quantities are described in Section 3.1.

2.2 Literature-Based Selection and Implementation of Control-Rod-Related Species

HERACLES-TDB does not include all species–phase combinations required to represent the absorber-related reaction pathways identified in the selected experiments. Control-rod-related species and phases are selected

based on experimentally identified reaction pathways and thermochemical data available in the literature. Species with available thermochemical properties are incorporated directly into HERACLES-TDB, whereas the data-deficient Cs–B–O species requiring a reaction-based representation are described separately in Section 2.3.

Representative SIC-related additions include Ag-I, Cd-I, Cs-Cd-I, and In-I species associated with metal–iodine pathways that can compete with CsI. Representative B_4C-related additions include B-C and B-O-H species associated with B_4C oxidation and the subsequent distribution of boron among gaseous and condensed species. The Cs–B–O extension additionally includes CsB_5O_8 and $Cs_2B_4O_7$ as cesium-bearing species relevant to boron-containing conditions. Because complete independent thermochemical data are unavailable for these species, their reaction-based representation is described separately in Section 2.3.

Species with available thermochemical data are implemented using standard-state thermodynamic and phase transition properties, with each phase treated as a separate species–phase combination. The extension comprises 19 chemical species and 43 species–phase combinations, as summarized in Table I.

Table I. Thermodynamic database extension

System	Chemical species	Species–phase combinations	Input basis
SIC-related	9	24	Thermochemical data
B_4C and B–O–H	6	13	Thermochemical data
Cs–B–O	4	6	Thermochemical and reaction-based data
Total	19	43	—

The extended database therefore enables equilibrium competition between CsI and absorber-related cesium-bearing species, including Cs–B–O species under boron-containing conditions, to be evaluated within a common calculation framework.

2.3 Reaction-Based Representation of Data-Deficient Cs–B–O Condensed Species

Thermochemical data are available for $CsBO_{2(s)}$, whereas complete standard-state thermochemical data are unavailable for $CsB_5O_{8(s)}$ and $Cs_2B_4O_{7(s)}$. Excluding these phases would remove the condensed Cs–B–O pathways available under boron-containing conditions and prevent the equilibrium calculation from representing competition between CsI and Cs–B–O phases for cesium. These phases are therefore represented using the following formation reactions, with $CsBO_{2(s)}$ and $B_2O_{3(l)}$ as reference species:

$$CsBO_2(s) + 2B_2O_3(l) = CsB_5O_8(s), \quad (2)$$

$$2CsBO_2(s) + B_2O_3(l) = Cs_2B_4O_7(s). \quad (3)$$

$CsB_5O_{8(s)}$ and $Cs_2B_4O_{7(s)}$ are treated as pure single-component solid phases with unit activity. In contrast, the activities of $CsBO_2$ and B_2O_3 used for the reactant terms are component activities in the pseudo-binary $CsBO_2$–B_2O_3 condensed system reported by Stolyarova et al. [12], referenced to the corresponding stable pure-component states at each temperature. The superscript PB denotes these pseudo-binary component activities, distinguishing them from the unit activities assigned to the pure product phases. Accordingly, the equilibrium constants of Eqs. (2) and (3) are expressed as

$$K_{CsB_5O_8} = \frac{a_{CsB_5O_8}}{a^{PB}_{CsBO_2}\,(a^{PB}_{B_2O_3})^2} = \frac{1}{a^{PB}_{CsBO_2}\,(a^{PB}_{B_2O_3})^2}, \quad (4)$$

$$K_{Cs_2B_4O_7} = \frac{a_{Cs_2B_4O_7}}{(a^{PB}_{CsBO_2})^2\,a^{PB}_{B_2O_3}} = \frac{1}{(a^{PB}_{CsBO_2})^2\,a^{PB}_{B_2O_3}}. \quad (5)$$

The a^{PB} values for $CsBO_2$ and B_2O_3 reported by Stolyarova et al. [12] at 800, 900, and 1,000 K are used to derive temperature-dependent equilibrium constants for Eqs. (2) and (3). Their temperature dependence is represented as

$$\log K_{CsB_5O_8}(T) = 5.283 - 1.20\times10^{-3}T, \quad (6)$$

$$\log K_{Cs_2B_4O_7}(T) = 18.34544 - 2.8971\times10^{-2}T + 1.32414\times10^{-5}T^2. \quad (7)$$

where T is expressed in kelvin. The corresponding standard Gibbs energy changes are obtained from

$$\Delta_r G^\circ(T) = -RT\ln K(T). \quad (8)$$

These values are combined with the thermodynamic properties of $CsBO_{2(s)}$ and $B_2O_{3(l)}$ to construct the temperature-dependent thermodynamic representations of $CsB_5O_{8(s)}$ and $Cs_2B_4O_{7(s)}$.

The activity data used for parameterization span 800–1,000 K; therefore, the reaction-based parameters are applied quantitatively within this temperature range. Calculations outside this range are used only to examine qualitative trends in thermodynamically favored species and are not interpreted as quantitative predictions of individual species fractions.

3. Results and Discussion

3.1 Evaluation Cases and Calculation Conditions

Equilibrium calculations are performed for selected conditions from CHIP #1/#2, TeRRa-RBS-1, and NUREG/CR-4963 Test 28, to evaluate CsI stability and iodine redistribution under Mo-, SIC-, and boron-containing chemical conditions. All experimental inputs are converted to molar quantities; flow-rate data are converted using residence times of 10 s for CHIP Phase I and 5 s for Test 28. The evaluated chemical systems, calculation conditions, and comparison quantities are summarized in Table II.

Table II. Calculation cases and comparison quantities

Case	Representative chemical system and condition	Comparison quantities
CHIP #1 and #2 [5,6]	Cs–I–Mo (#1); Cs–I–Mo–Ag–Cd (#2) Phase I (transport): 423–1873 K; Phase II (revaporization): 423–723 K	Elemental inventory ratios; I species fractions
TeRRa-RBS-1 [7]	Cs–I–B; revaporization: 850 K	CsI conversion; Cs/I species fractions
NUREG/CR-4963 Test 28 [8]	Cs–I–B–C; high-temperature reaction: 1270 K	Cs/I/B species fractions; elemental balances

For CHIP Phase I, elemental inventory ratios derived from the converted inputs are compared with the whole-line experimental inventories because the present equilibrium model does not resolve spatial deposition profiles. Phase II is assessed using iodine phase and species distributions under the reported revaporization conditions. The converted CHIP Phase I compositions differ from the reported whole-line Cs/I, Cd/I, Ag/I, Mo/Cs, and Mo/Cd ratios by 0.25–5.05%, within the reported uncertainty of 8–10% for elemental mass determination [5,6]. This comparison provides an input-consistency check for the equilibrium calculations.

TeRRa-RBS-1 is evaluated as a local equilibrium state at the 850 K deposition location by comparing the calculated CsI conversion with the measured decrease in the iodine deposits. NUREG/CR-4963 Test 28 is assessed using the distributions of Cs-, I-, and B-bearing species and the corresponding cumulative elemental balances.

Because the experiments differ in bulk composition, temperature, and the physical state of the supplied CsI, numerical species fractions are compared only within each experimental condition. Cross-case comparisons are therefore used to interpret qualitative differences in cesium and iodine partitioning rather than to compare species fractions directly.

3.2 CsI Stability and Iodine Redistribution under SIC-Related Conditions

Under the CHIP #1 Phase I condition, non-CsI iodine species increase over the temperature range in which cesium molybdate species become stable, as shown in Fig. 1. Cesium partitioning into Cs–Mo–O species reduces CsI formation and shifts iodine toward $I_{2(g)}$, $I_{(g)}$, and $HI_{(g)}$. These results indicate that competition between CsI and cesium molybdate controls the calculated iodine distribution under the CHIP #1 condition.

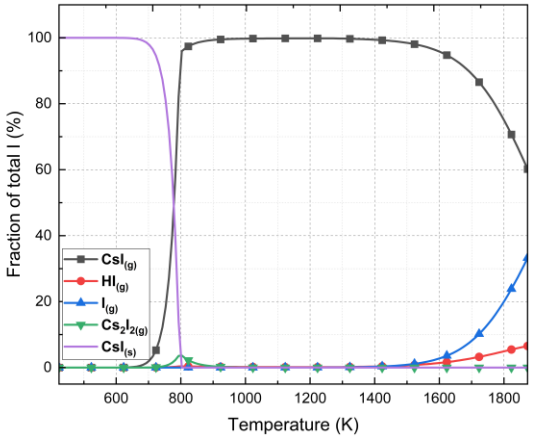


Fig. 1. Calculated iodine species fractions for CHIP #1 under Phase I conditions

For CHIP #2 Phase I, CsI remains predominant over a wider temperature range, while non-CsI iodine species remain limited, as shown in Fig. 2. Unlike CHIP #1, where cesium molybdate formation redistributes cesium away from CsI, the Ag- and Cd-containing system maintains a stronger association between cesium and iodine over most of the evaluated temperature range. The Ag- and Cd-containing system therefore exhibits a different equilibrium partitioning behavior, with a more CsI-centered distribution. This tendency is consistent with the experimentally reported reduction in gaseous iodine transport in the presence of SIC-related constituents [6].

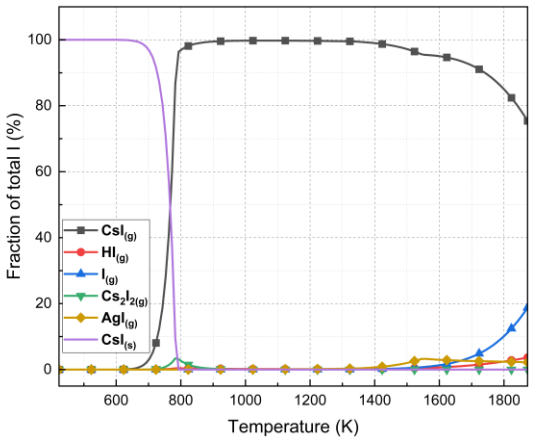


Fig. 2. Calculated iodine species fractions for CHIP #2 under Phase I conditions

The Phase II results further distinguish between the two chemical systems. Under the CHIP #1 condition, iodine is predominantly distributed to the gas phase as $I_{2(g)}$, whereas cesium and molybdenum remain in condensed species, as shown in Fig. 3. At 573 K, the calculated condensed-phase retention fractions of both cesium and molybdenum are 100%, differing from the reported values by 0.02 and 0.03 percentage points, respectively [5]. The simultaneous retention of cesium and molybdenum in the condensed phase and gas-phase partitioning of iodine, together with the stability of Cs–

Mo–O condensed species, indicate a thermodynamic tendency for iodine to separate from the deposited material under the oxidizing steam–air condition.

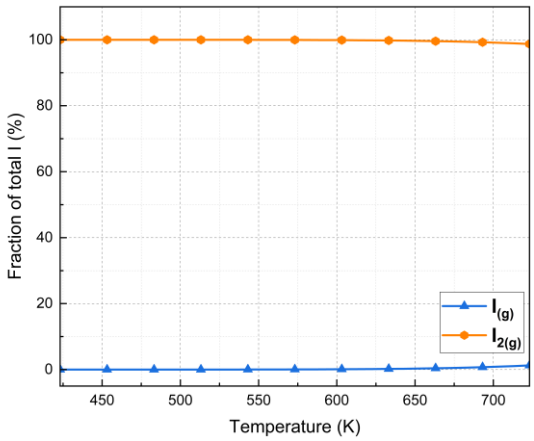


Fig. 3. Calculated iodine species fractions for CHIP #1 under Phase II conditions

In contrast, $CsI_{(s)}$ remains the predominant iodine species throughout the CHIP #2 Phase II temperature range, as shown in Fig. 4. The calculated gas-phase iodine fraction is negligible at 443 and 573 K and approximately 0.01% at 723 K. Consequently, approximately 99.99% of the iodine inventory remains in the condensed phase even at 723 K. The persistence of $CsI_{(s)}$ indicates that the Ag- and Cd-containing system maintains the association between cesium and iodine under the evaluated revaporization conditions, consistent with the reduced gaseous iodine transport reported for CHIP #2 [6].

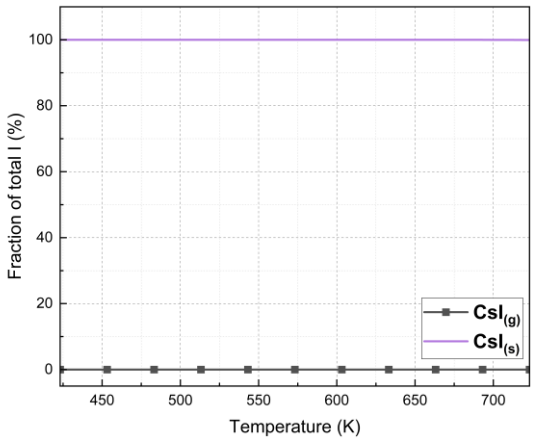


Fig. 4. Calculated iodine species fractions for CHIP #2 under Phase II conditions

Taken together, the results indicate that the contrasting iodine partitioning observed in CHIP #1 and #2 can be interpreted by competition among cesium-bearing phases: cesium molybdate formation reduces CsI stability in the Mo-containing system, whereas CsI remains thermodynamically favored in the Ag- and Cd-containing system.

3.3 CsI Conversion and Iodine Redistribution under Boron-Containing Conditions

Under the TeRRa-RBS-1 steam–boron condition, 74.1% of the initial cesium inventory is distributed to $CsB_5O_{8(s)}$ at 850 K, while 25.9% remains as $CsI_{(s)}$, as shown in Fig. 5. The stabilization of $CsB_5O_{8(s)}$ provides a competing condensed-phase sink for cesium, reducing the fraction retained as CsI.

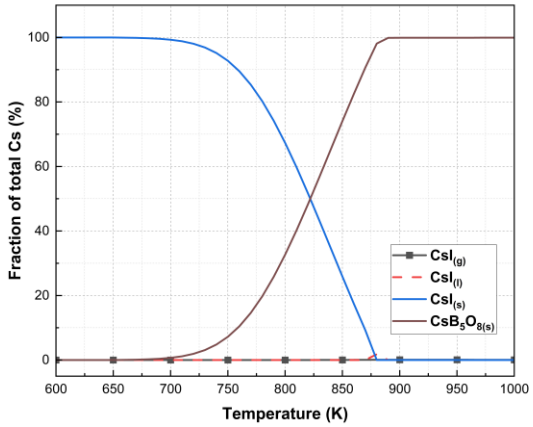


Fig. 5. Calculated cesium species fractions under the TeRRa-RBS-1 steam–boron condition

Correspondingly, 74.0% of the initial iodine inventory is distributed to gaseous $HI_{(g)}$, $I_{2(g)}$, and $I_{(g)}$, whereas 25.9% remains as $CsI_{(s)}$, as shown in Fig. 6. Because cesium is partitioned almost entirely between CsI and CsB_5O_8 under this condition, the fraction transferred to CsB_5O_8 directly represents the calculated CsI conversion. Given the 1:1 Cs-to-I molar ratio in CsI, this conversion also corresponds to the fraction of iodine removed from CsI in the local equilibrium calculation. The resulting CsI conversion of 74.1% lies within the uncertainty range of the experimentally measured 76.1 ± 6.4% decrease in the iodine deposit near 850 K [7]. This consistency supports the calculated local redistribution trend from CsI to $CsB_5O_{8(s)}$ under the evaluated condition.

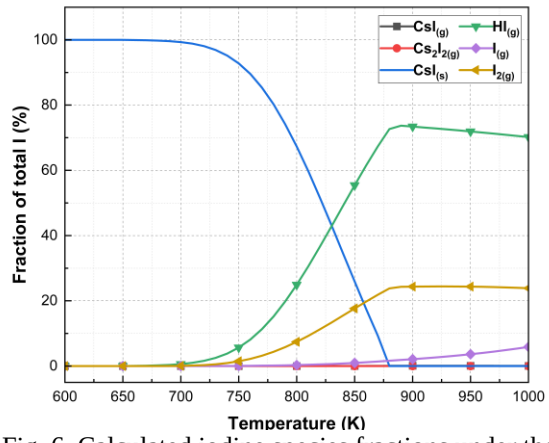


Fig. 6. Calculated iodine species fractions under the TeRRa-RBS-1 steam–boron condition

Under the NUREG/CR-4963 Test 28 condition at 1270 K, 82.2% of the cesium inventory is distributed to $CsBO_{2(g)}$, while 16.9% remains as $CsI_{(g)}$, as shown in Fig. 7. $CsOH_{(g)}$ and $(CsBO_2)_{2(g)}$ account for 0.5% and 0.3%, respectively. The calculated redistribution of cesium toward Cs–B–O species is qualitatively consistent with the experimental observation of cesium, with little iodine, in the boron oxide layer formed on the B_4C specimens [8].

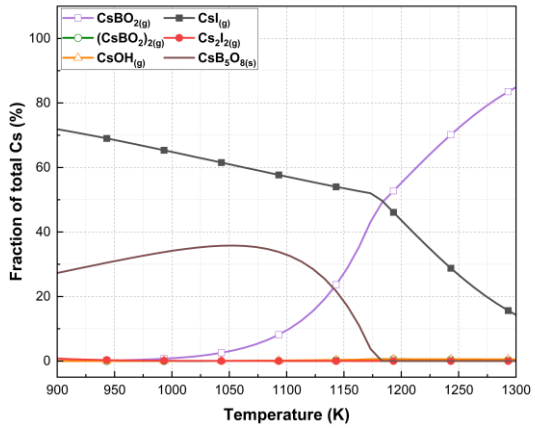


Fig. 7. Calculated cesium species fractions under the NUREG/CR-4963 Test 28 condition

The corresponding iodine distribution is dominated by non-CsI gaseous species. As shown in Fig. 8, 59.8% of the iodine inventory is distributed to $HI_{(g)}$, 23.3% to $I_{(g)}$, and 16.9% remains as $CsI_{(g)}$. $I_{2(g)}$ and other minor iodine species together account for less than 0.01%, resulting in a total non-CsI iodine fraction of 83.1%. Although the detailed calculated species fractions are not directly validated against Test 28, the Cs–B–O distribution is dominated by $CsBO_{2(g)}$, consistent with the $CsBO_2$-centered product pathway proposed for the experiment, and is accompanied by HI-dominated iodine partitioning [8].

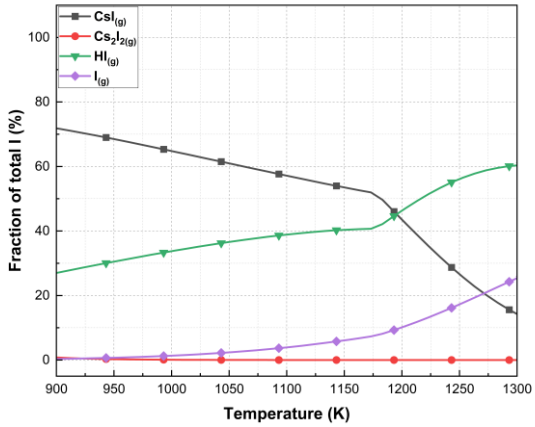


Fig. 8. Calculated iodine species fractions under the NUREG/CR-4963 Test 28 condition

The cumulative material balances for Test 28 show relative differences of −5.4% to −0.2% between the selected calculated and experimental quantities [8]. The calculated transported boron amount is 2.57 g-B, which is 1.9% lower than the experimental value. The iodine supplied as CsI is calculated as 28.93 mg-I, corresponding to a difference of −0.2%, while the calculated iodine amount contained in $HI_{(g)}$ is 17.31 mg-I, 5.4% lower than the experimentally recovered total iodine amount. These comparisons provide integral checks against selected reported boron and iodine material-balance quantities rather than species-specific validation of the 1270 K equilibrium distribution.

TeRRa-RBS-1 represents deposited CsI interacting with boron-bearing steam at 850 K, whereas Test 28 represents gaseous CsI interacting with B_4C–steam reaction products at 1270 K. Under these conditions, $CsB_5O_{8(s)}$ is stabilized as a condensed cesium-bearing phase in TeRRa-RBS-1, while $CsBO_{2(g)}$ is predominant in Test 28. Despite the different stable Cs–B–O species, both calculations show that cesium partitioning into Cs–B–O species decreases the fraction retained as CsI and increases non-CsI gaseous iodine.

Although selected cumulative material balances are compared quantitatively, the detailed species partition at 1270 K is interpreted primarily as a thermodynamic trend because the reaction-based Cs–B–O parameters are derived from activity data at 800–1000 K.

3.4 Thermodynamic Interpretation of Control-Rod-Material-Dependent CsI Stability

The results can be interpreted through the competing cesium-bearing pathways available under each control-rod-related chemical condition. CsI remains stable when cesium is preferentially associated with iodine. When alternative Cs-bearing species become stable, cesium is redistributed away from CsI and iodine is correspondingly partitioned into non-CsI species.

Under the SIC-related conditions, the Mo–Cs–I system in CHIP #1 allows cesium molybdate formation to compete with CsI, while iodine is partitioned into non-CsI species. The Ag- and Cd-containing CHIP #2 system remains more CsI-centered under both transport and revaporization conditions. Under the boron-containing conditions, $CsB_5O_{8(s)}$ and $CsBO_{2(g)}$ act as alternative cesium-bearing products. Their formation reduces the fraction of cesium retained as CsI and increases the partitioning of iodine into non-CsI gaseous species.

The evaluated experiments involve different compositions, temperatures, atmospheres, and physical states of CsI; therefore, their numerical species fractions are not directly compared. Instead, the results identify a common thermodynamic relationship in which CsI stability depends on the competitive partitioning of cesium among the Cs-bearing species permitted by the surrounding chemical system. The extended database therefore provides a thermodynamic basis for

interpreting condition-dependent CsI stability and iodine redistribution under SIC- and B_4C-related conditions.

4. Conclusion

This study extended HERACLES-TDB to represent the SIC- and B_4C-related reaction pathways required to examine CsI stability and iodine redistribution. The extension combined literature-based thermochemical data for control-rod-related species with reaction-based representations of data-deficient Cs–B–O condensed phases. Across the evaluated conditions, CsI stability decreased when alternative cesium-bearing species became thermodynamically favorable, whereas the Ag- and Cd-containing CHIP #2 system remained more CsI-centered than the Mo–Cs–I system in CHIP #1. The absorber-related differences in the calculated iodine distributions were therefore interpreted through the competitive partitioning of cesium among the species permitted by each chemical system.

The case-specific comparisons provided supporting evidence for this thermodynamic interpretation within the defined scope of each experiment. For TeRRa-RBS-1, the calculated CsI conversion of 74.1% was within the uncertainty range of the measured 76.1 ± 6.4% decrease in the iodine deposits near 850 K, supporting the calculated redistribution of cesium from CsI to Cs–B–O phases. For NUREG/CR-4963 Test 28, the differences between selected calculated and experimental cumulative material-balance quantities ranged from −5.4% to −0.2%, providing an integral consistency check on the calculated redistribution. However, because the Test 28 temperature of 1270 K was outside the 800–1000 K range used to derive the reaction-based Cs–B–O parameters, the detailed species fractions were interpreted as thermodynamic redistribution trends rather than as direct quantitative predictions.

The extended thermodynamic database therefore provides a common framework for evaluating condition-dependent CsI stability and iodine redistribution across SIC- and boron-containing chemical systems. Such chemical-speciation information could support source-term assessments in which iodine transport and retention depend on its chemical form. The present calculations represent spatially lumped equilibrium states and do not resolve reaction kinetics, transport, deposition, or time-dependent revaporization. Further work should improve the high-temperature thermodynamic and phase data for the Cs–B–O system and couple equilibrium speciation with kinetic and transport models in integrated severe-accident analyses.

ACKNOWLEDGEMENTS

This study was supported by the Nuclear Safety Research Program through the Regulatory Research Management Agency for SMRs (RMAS) and the Nuclear Safety and Security Commission (NSSC) of the Republic of Korea. (No. RS-2025-02311309)

REFERENCES

[1] L. Soffer, S. B. Burson, C. M. Ferrell, R. Y. Lee, and J. N. Ridgely, *Accident Source Terms for Light-Water Nuclear Power Plants*, NUREG-1465, U.S. Nuclear Regulatory Commission, 1995.
[2] U.S. Nuclear Regulatory Commission, *Technical Bases for Estimating Fission Product Behavior During LWR Accidents*, NUREG-0772, 1981.
[3] B. Clément and R. Zeyen, “The objectives of the Phébus FP experimental programme and main findings,” Annals of Nuclear Energy, Vol. 61, pp. 4–10, 2013.
[4] B. Simondi-Teisseire, N. Girault, F. Payot, and B. Clément, “Iodine behaviour in the containment in Phébus FP tests,” Annals of Nuclear Energy, Vol. 57, pp. 157–169, 2013.
[5] A.-C. Grégoire et al., “Studies on the role of molybdenum on iodine transport in the RCS in nuclear severe accident conditions,” *Annals of Nuclear Energy*, Vol. 78, pp. 117–129, 2015.
[6] A.-C. Grégoire et al., “Influence of SIC control rod material on the iodine release in case of nuclear severe accident—Chemical reactivity with fission products in thermal conditions of RCS,” *Annals of Nuclear Energy*, Vol. 168, 108900, 2022.
[7] M. Rizaal, S. Miwa, E. Suzuki, J. Imoto, M. Osaka, and M. Gouëllo, “Revaporization behavior of cesium and iodine compounds from their deposits in the steam–boron atmosphere,” *ACS Omega*, Vol. 6, pp. 32695–32708, 2021.
[8] R. M. Elrick, R. A. Sallach, A. L. Ouellette, and S. C. Douglas, *Boron Carbide–Steam Reactions with Cesium Hydroxide and with Cesium Iodide at 1270 K in an Inconel 600 System*, NUREG/CR-4963, SAND87-1491, Sandia National Laboratories, 1987.
[9] D. A. Kulik, T. Wagner, S. V. Dmytrieva, G. Kosakowski, F. F. Hingerl, K. V. Chudnenko, and U. R. Berner, “GEM-Selektor geochemical modeling package: Revised algorithm and GEMS3K numerical kernel for coupled simulation codes,” Computational Geosciences, Vol. 17, pp. 1–24, 2013.
[10] Paul Scherrer Institute, “GEMS specific HERACLES v.0.2 database for U, TRU and FP speciation,” available at the Paul Scherrer Institute HERACLES database website, accessed Jan. 29, 2026.
[11] M. Suzuki, K. Kurosaki, S. Yamanaka, T. Tanaka, M. Uno, Y. Murakami, T. Jantzen, S. Petersen, and K. Hack, “Development of thermodynamic databases in the system U–Zr–Ce–Cs–Fe–B–C–I–O–H for application to simulating phase equilibria in severe nuclear accidents,” Journal of Nuclear Science and Technology, Vol. 55, No. 8, pp. 885–899, 2018.
[12] V. L. Stolyarova, V. A. Vorozhtcov, S. I. Lopatin, S. M. Shugurov, E. P. Simonenko, N. P. Simonenko, M. Kurata, and D. Costa, “High-temperature mass spectrometric study of vaporization and thermodynamics of the Cs_2O–B_2O_3 system: Review and experimental investigation,” Rapid Communications in Mass Spectrometry, Vol. 35, No. 11, e9079, 2021.